Earth and Planetary Science Letters 572 (2021) 117117

Contents lists available at ScienceDirect

Earth and Planetary Science Letters

www.elsevier.com/locate/epsl

Effective seismic wave velocities and attenuation in partially molten rocks

Vladimir Lyakhovsky [a,*], Eyal Shalev [a], Ittai Kurzon [a], Wenlu Zhu [b], Laurent Montesi [b], Nikolai M. Shapiro [c,d]

[a] Geological Survey of Israel, Jerusalem, Israel
[b] Department of Geology, University of Maryland, College Park, MD, USA
[c] Institut de Sciences de la Terre, Université Grenoble Alpes, CNRS (UMR5275), CS 40700, 38058 Grenoble Cedex 9, France
[d] Schmidt Institute of Physics of the Earth, Russian Academy of Sciences, Bolshaya Gruzinskaya str., 10-1, 123242 Moscow, Russia

ARTICLE INFO

Article history:
Received 16 March 2021
Received in revised form 6 July 2021
Accepted 16 July 2021
Available online xxxx
Editor: H. Thybo

Keywords:
partial melt
phase transition
wave velocity
attenuation

ABSTRACT

Significant reduction in mechanical properties, i.e., elastic moduli and seismic wave velocities, as well as enhanced inelastic attenuation is often associated with areas of partially molten rocks. In this paper we suggest a new mechanism responsible for significant reduction of wave velocity and enhanced attenuation. The suggested mechanism considers solid-melt phase transition at thermodynamic equilibrium. Any pressure change, that takes the system out of thermodynamic equilibrium, causes solidification or melting which modifies the heat balance according to the Clausius-Clapeyron equation. The latent heat (sink or source) is transferred away or towards the interface by conductive-advective mechanism, heating or cooling the entire rock mass, and leading to energy loss and dissipation of the mechanical energy and to seismic wave attenuation. We use simplified geometry and derive analytical solutions for wave velocity reduction and attenuation associated with a moving solid-melt interface (Stefan problem). We demonstrate that the latent heat generation due to wave-induced pressure oscillations around thermodynamic equilibrium is an efficient mechanism for energy dissipation and leads to significant reduction in mechanical properties (seismic velocities and attenuation). The highest attenuation occurs when the period of oscillation is close to the heat transfer time-scale associated with the size of melt inclusions. The predicted values are approximately in agreement with large scale seismological observations, showing that seismic waves are mostly attenuated within the shallow parts of Earth's crust and mantle, and are associated with possible presence of melt.

1. Introduction

Melts are largely present in the crust and uppermost mantle of the Earth. The partially molten rocks are characterized by enhanced mobility because of their elevated buoyancy and reduced viscosity and, therefore, play a key role in many geodynamical processes. Partial melting of silicate rocks occur in regions within the crust and in the uppermost mantle where the solidus-liquidus transition can be reached by different mechanisms such as: decompression (e.g., Niu, 1997), heating by uprising hot material such as mantle plumes (e.g., Campbell, 2005), compositional changes such as the addition of water (e.g., Asimow and Langmuir, 2003), or by mechanical processes such as frictional melting (e.g., (Di Toro et al., 2006). The most direct manifestations of the presence of the molten rocks are the volcanic deposits observed at the surface, and the magmatism imprinted in geological records. Initial magmas form at depths and driven by buoyancy, rise toward the surface, through the uppermost mantle and the crust. While volcanic deposits of molten rock reach the surface, most of the magmas and molten rock remain stored at depth. Understanding how the magma and molten rocks are stored at depth is one of the major challenges in volcanology and igneous geology. Traditional views, implying the existence of concentrated "high-melt" volumes, forming well identified intrusions or magma chambers, is challenged today with new concepts suggesting a more distributed storage of melts in a form of low melt-fraction "mush reservoirs" (Jackson et al., 2018). The form of such storage at depth strongly affects the evolution of magmas/melts and their mobility, changing the hydraulic connectivity of volcano-magmatic systems (Pinel et al., 2010). Melt distribution within the shallow layers of the crust is of great importance for estimating the potential volcanic activity. Estimation of the volume of erupted volcanic products from geo-

* Corresponding author.
E-mail address: vladimir.lyakhovsky@gmail.com (V. Lyakhovsky).

https://doi.org/10.1016/j.epsl.2021.117117
0012-821X/

logical records shows that past rates of volcanism were very variable both for individual volcanic systems and for the whole Earth. In particular, the level of volcanic activity that occurred during human history is rather weak compared to some pre-human major events such as explosive super-Plinian eruptions, the emergence of flood basalts and the generation of large igneous provinces (e.g., Bryan et al., 2010); such strong events are often called upon to explain environmental changes and mass extinctions (Sobolev et al., 2011). The possibility of occurrence of new major volcanic episodes with great impact at a global scale cannot be excluded and its understanding requires the estimation of melt distribution within the shallow layers of the crust.

The presence of melt is also of major importance for global mantle dynamics and plate tectonics. Mantle convection in the vicinity of the major convergent and divergent plate boundaries is strongly influenced by the melt fraction, present in the subduction zone mantle wedges (e.g., Gerya and Meilick, 2011) and beneath the mid-oceanic ridges (e.g., Niu, 1997). Partial melts are also suggested to contribute significantly to the mechanical weakness of the asthenosphere (e.g., Chantel et al., 2016) and to facilitate the widespread small-scale sub-lithospheric convection (e.g., van Hunen et al., 2005). Partial melting might be present in the continental crust driving fast deformation of the rocks, and affecting the orogenesis (Chen et al., 2018). Also, partial melts can lubricate seismogenic faults (Di Toro et al., 2006) and, therefore, affect earthquake dynamic and seismo-tectonic cycles.

Understanding many ongoing key geodynamic processes and related natural hazards requires information on the distribution of partial melt storage systems and reservoirs in the Earth's crust and upper mantle. This information can be obtained only by methods of deep geophysical sounding, searching for the areas with abnormal physical and mechanical properties. One possible approach is finding the presence of partial melt in the subsurface by searching for elevated electrical conductivity (Watanabe and Kurita, 1993). So far, large scale electromagnetic and magneto-telluric surveys were used to study partially molten rocks located at depths beneath mid oceanic ridges (e.g., Baba et al., 2006) and volcanoes (e.g., Hill et al., 2009).

Another approach is to use the significant reduction in mechanical properties, i.e., elastic moduli and seismic wave velocities, as well as enhanced anelastic attenuation in the areas with partially molten rocks that can be measured with different seismological methods (Debayle et al., 2020). This approach is much widely used because of the existence of numerous permanent and temporary seismic networks. In highly active volcanic systems the mobility of melt can lead to recordable seismic radiation (Chouet, 1996; Shapiro et al., 2017). However, in most cases, the detection of molten rocks requires using different methods of seismic imaging. Since it is widely accepted that the shear modulus and S-wave velocity are most affected by the presence of melt (or more generally fluid fraction), the S-wave seismic tomography is particularly suitable to image the regions with presence of significant portions of melt such as in mid-oceanic ridges (e.g., Conder et al., 2002) or hotspots (Allen et al., 2002). Strong negative P-wave seismic velocity anomalies can also indicate the presence of melt, especially beneath volcanoes, and in many cases, the Vp/Vs ratio is used to trace the melts (e.g., Koulakov et al., 2020). Melt-induced variations of the elastic moduli also affect the reflectivity structure in the crust and in the uppermost mantle. Therefore, the melt-enriched regions can be imaged with seismic reflection methods or with its passive seismology analog: the receiver functions (e.g., Rychert et al., 2013). Different methods of attenuation measurement using amplitudes of direct waves (P, S) and the coda of seismograms can be used in different geological settings (e.g., Prudencio and Manga, 2020). The separation of the intrinsic attenuation and scattering is a particularly challenging issue. The latter can be strongly enhanced by the presence of small pockets of partially molten rocks.

As mentioned above (Jackson et al., 2018), magma and melt may be stored not within large intrusions or reservoirs but rather distributed over a system of small melt pockets or layers with dimensions smaller than seismic wavelengths. In such cases, the preferred orientation of these small partially molten volumes may result in seismic anisotropy. This mechanism can contribute to the well-known radial seismic anisotropy in the upper mantle (Ekström and Dziewonski, 1998). More recently, radial seismic anisotropy has been discovered beneath some large volcanic systems (e.g., Jaxybulatov et al., 2014) where it is believed to be caused by the presence of large sill complexes, composed of many nearly horizontal layers of magmatic rocks with different degree of partial melting.

Interpretation of the seismological observations requires understanding of the effects of the properties of the partially molten rocks on the melt fraction and topology of melt inclusions. Zhu et al. (in preparation) approach this problem by numerical simulations of the effective elastic properties of different samples prepared in laboratory from a powder mixture of natural basalt with a wide range of melt fraction values. They demonstrate that in-spite of the complex topology of melt distribution, the simple geometrical model of the elastic media, using spherical fluid inclusions, provides a good approximation for the mechanical behavior of the solid-fluid system. However, their static modeling, similar to most of the previous studies, ignores the impact of heat and mass transport across the solid-melt interface associated with pressure oscillations. We utilize the simple geometry of spherical melt inclusions and develop an analytical solution predicting the impact of the solid-melt phase transition on the bulk elasticity and wave attenuation.

In the next section we briefly review averaging models for effective properties of partially molten rocks. Later we provide key aspects of the existing mechanical models of partially molten rocks. Then we discuss the technique of sample preparation and the applied numerical method. Section 4 describes results of numerical simulations and their comparison with existing models of effective elasticity of partially molten rocks (see Appendix A for model details). Then we summarize the main relations connecting bulk elasticity and wave attenuation with moving boundary between solid and melt phases. The detailed derivations are presented in Appendix B. Our findings lead to practical suggestions that may improve the interpretation of seismological observations in areas with partially molten rocks.

2. Effective properties of Partially Molten Rocks

2.1. Bulk elasticity and seismic wave velocities

A partially molten rock is a composite material with solid and liquid (melt) fractions. Effective elastic properties of composite materials have been studied for decades starting with original works by Voigt (1890) and Reuss (1929) who suggested upper and lower bound values for any given volume fraction of constituents, ignoring the topology of the partially molten rock (see Appendix A for detailed description of these and other models). The Voigt (1890) iso-strain model assumes that all constituents have the same strain and provides the upper bound value, while the Reuss (1929) iso-stress assumption leads to the lower bound value. In the case of the solid-melt system with zero shear modulus of the liquid phase, the lower bound value for the shear modulus is zero. Converting elastic moduli to V_p and V_s values allows estimating their expected reduction as a function of the melt fraction (Fig. 1). The expected reduction of the V_p values is relatively minor, smaller than 20% velocity reduction for melt fractions of up

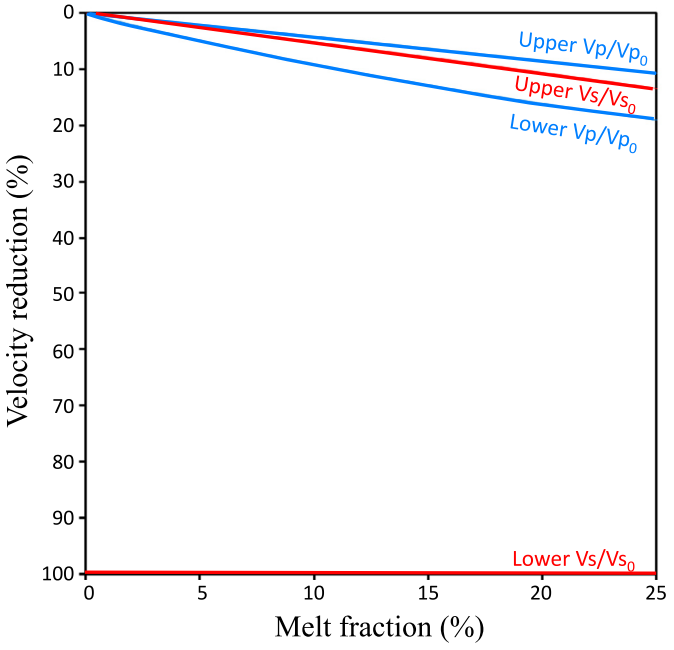

Fig. 1. Upper and lower bounds for velocity reduction according to the iso-strain (Upper) and iso-stress (Lower) models, for both, Vp (blue) and Vs (red) seismic velocities. (For interpretation of the colors in the figure(s), the reader is referred to the web version of this article.)

to 25% (blue curves in Fig. 1). However, the possible range of V_s values is large (red curves in Fig. 1). The iso-strain, Voigt model predicts only minor reduction, whereas the iso-stress model predicts zero V_s values. This wide range is not useful for practical applications and cannot be used to constrain the melt fraction. The Hashin–Shtrikman–Walpole models provide more realistic bounds, giving the narrowest possible range of bulk elasticity without specifying the geometries of the melt inclusions. Several models considered sphere or ellipsoid inclusion shape and developed analytical solutions (equations a3-a5, Appendix A), connecting effective elastic properties with melt fraction. Several numerical methods, such as self-consistent and differential effective medium methods, were proposed to account for inclusion interaction and wide range of possible geometries. These methods as well as more accurate evaluation of the effective elastic properties achieved by characterization of the microstructure geometry are briefly discussed in Appendix A.

2.2. Wave attenuation

Quantitative interpretation of seismic wave attenuation in partially molten rocks addresses two general mechanisms. One mechanism considers viscous dissipation due to melt flow or squirt flow in thin films (e.g., Mavko et al., 2009; O'Connell and Budiansky, 1977). Another mechanism addresses dislocation-diffusion stress relaxation in distributed melt pockets or inclusions (e.g., Karato and Spetzler, 1990; Morris and Jackson, 2009). Both approaches were examined in theoretical and laboratory studies, using natural rocks and synthetic materials, quantifying the seismic attenuation, and trying to establish a physical understanding of these mechanisms (Faul and Jackson, 2015; Yamauchi and Takei, 2016). Each approach has its shortcomings; while viscous dissipation, due to melt flow, requires unrealistically high melt viscosity (Faul and Jackson, 2015), the dislocation-diffusion mechanism does not explain the strong association of attenuation with the onset of melting (Fontaine et al., 2005).

The relaxation time for a melt-squirt within elliptical inclusions was derived by (O'Connell and Budiansky, 1977). In the case when fluid fills narrow crack-like zones, the scaling relations should account for the crack aspect ratio, or the ratio between opening and length (c/a). They concluded that the most efficient attenuation of fluid-saturated cracked solids is expected for a frequency range defined by two bounding frequencies:

$$\omega_1 = \frac{K}{\eta}\left(\frac{c}{a}\right)^3 \quad \text{and} \quad \omega_2 = \frac{\mu}{\eta}\left(\frac{c}{a}\right) \tag{1}$$

This frequency range, as well as the general time scale for the transient deformation, is associated with the stress relaxation process characterized by the Maxwell relaxation time, defined as the ratio between fluid viscosity and elastic modulus of the rock mass. Viscosity of dacites and rhyolitic melts, that are expected to be present in the magmatic systems of the continental crust, is relatively high. The viscosity of rhyolites may be as high as 10^{11} Pa s for dry melts and decrease to about 10^6 Pa s depending on water content. The Maxwell relaxation time for these melts is of the order of 10^{-3}-10^{+2} s, overlapping the seismological frequency range. Therefore, the analysis of fluid-filled cracks of O'Connell and Budiansky (1977) could well encompass the seismological observations for dacites and rhyolitic melts. However, for typical viscosity range of basaltic melts is 10^0-10^2 Pa s and their elastic modulus is of the order of tens GPa; hence, their Maxwell relaxation time is of the order of 10^{-7}-10^{-9} s, and the effects associated with visco-elastic relaxation are negligibly small, after very short time intervals. Accordingly, we may expect significant attenuation only at very high frequency waves. More accurate estimation (eq. (1)) predicts that even for a small aspect ratio $c/a \sim 10^{-2}$, the typical frequency range is above 1 KHz, which is well above the seismological frequency range. This was already noted by Mavko, 1980 and Mavko et al. (2009), who also discussed squirt flow mechanism.

These estimations are compatible with results discussed by Faul et al. (2004) who noted that experimentally observed attenuation in melt-bearing olivine polycrystals reported by Jackson et al. (2004) is not compatible with melt squirt flow through an observed small pipe with aspect ratios around $c/a \sim 10^{-1}$. They also noted that this flow mechanism requires unrealistically high melt viscosity ($\sim 10^4$ Pa s). Faul et al. (2004) suggested an alternative stress relaxation mechanism introducing effective viscosity for olivine-olivine grain boundary regions. Adjusting high "grain-boundary viscosities" ($\sim 10^6$ Pa s) allow fitting the observed attenuation; however, the background physical mechanism, responsible for temperature-dependent attenuation, is still not clear.

In addition, most of the recent works discuss different mechanisms for shear attenuation and neglect bulk attenuation. Vaišnys (1968) and Mavko (1980) discussed the mechanism of bulk attenuation and noted the role of the phase transition between solid and melt phases due to wave-induced pressure oscillations. Li and Weidner (2008) reported results of a complicated laboratory measurement demonstrating effects associated with the presence of phase changes. Their results support the velocity decrease and bulk attenuation observed during loading with a period of 1,000 s and the softening observed at low amplitudes and shorter periods. Ricard et al. (2009) and Durand et al. (2012) investigated seismic wave attenuation due to solid-solid phase transformation. They considered finite rate of kinetics, but without latent heat generation. Their model successfully predicted seismic mode attenuation associated with phase transition at 410 km depth (Durand et al., 2012). However, this attenuation mechanism is not very efficient for body waves with typical frequency range 0.1–1 Hz. In the case of the solid-melt phase transition, the characteristic time scale of the heat transport generated at the solid-melt interface (latent heat) varies between milliseconds to tens of seconds for melt inclusions of sizes, ranging from tens of microns to centimeters scale (Mavko, 1980). Because latent heat is very efficient in releasing energy, it may cause significant attenuation. In this study we develop

the analytical solution predicting the impact of the heat generated at the solid-melt phase transition on the bulk elasticity and wave attenuation, considering infinitely fast kinetics.

3. Method

3.1. Bulk elasticity, no mass/heat transfer

Zhu et al. (2011) obtained high-resolution 3-D determinations of melt distribution in experimentally produced olivine-basalt aggregates using X-ray synchrotron microtomography. Olivine-basalt aggregates with melt fractions of 0.02, 0.05, 0.10, and 0.20 were synthesized from powder mixtures of pulverized natural forsterite and Mid Ocean Ridge Basalts (MORB). The spatial resolution of the synchrotron microtomographic images is ~0.7 microns. Comparison to the conventional 2-D scanning electron microscopy (SEM) images of the same samples demonstrated that the microtomographic method captured realistic melt distribution in 3-D, over a large representative volume (Zhu et al., 2011). More information regarding the experimental details and the image analysis could be found in (Miller et al., 2014).

Using the reported 3-D melt geometries, Zhu et al. (in preparation) recently conducted finite element deformation experiments to obtain the effective bulk and shear moduli of these experimental charges. In the numerical simulations, the numerical elements were dictated by the pixel size of the tomography image with every pixel represented by a cubic brick separated into five tetrahedron elements. The grid avoids any smoothing or averaging of the observed microstructure. The material properties of each pixel (set of five tetrahedron elements) are defined as solid or melt according to the tomographic image. Following (Hammond and Humphreys, 2000), we use $K_S = 124$ GPa, $K_M = 64$ GPa, and $\mu_S = 40$ GPa (solid Poisson ratio is 0.28). Infinite viscosity (zero fluidity) is defined for the solid phase, while typical viscosity of 10 Pa s and zero shear modulus are adopted for the melt phase. The viscous strain component act to dampen deformation and facilitates the numerical transient phase that goes from the initial un-deformed equilibrium state to the final static deformed equilibrium state. Boundary conditions for every model run are set according to the simulated loading, i.e., 3-D compaction or uniaxial load. Static stress distribution is simulated using our 3-D code, utilizing Fast Lagrangian Algorithm, verified in many previous studies.

The actual melt fraction, calculated for every sub-volume, depends on the amount of melt generated in the original laboratory sample, and also varies between different sub-volumes of the same sample, representing the heterogeneity and complex topology of the melt distribution. The lack of any clustering or any preferred location of markers in Fig. 2, corresponding to the size of the numerical grid (100, 200, 300, and 400 pixels), confirms that the obtained results are robust and there is no meaningful grid dependency. Colored lines in Fig. 2 show effective elastic moduli predicted by different analytical models discussed in Appendix A. Results of numerical simulations of the effective elastic properties demonstrate that the simple geometrical model, elastic media with spherical melt inclusions, provide the most reliable approximation for the mechanical behavior of the solid-fluid system, in spite of the very simplified topology. This topology of the melt distribution, in a form of spherical inclusions located each in the center of equal cells (schematically shown in Fig. 3) predicts surprisingly well the elastic properties of partially molten rocks, and will be used in the next section to study impact of heat and mass transport across the solid-melt interface.

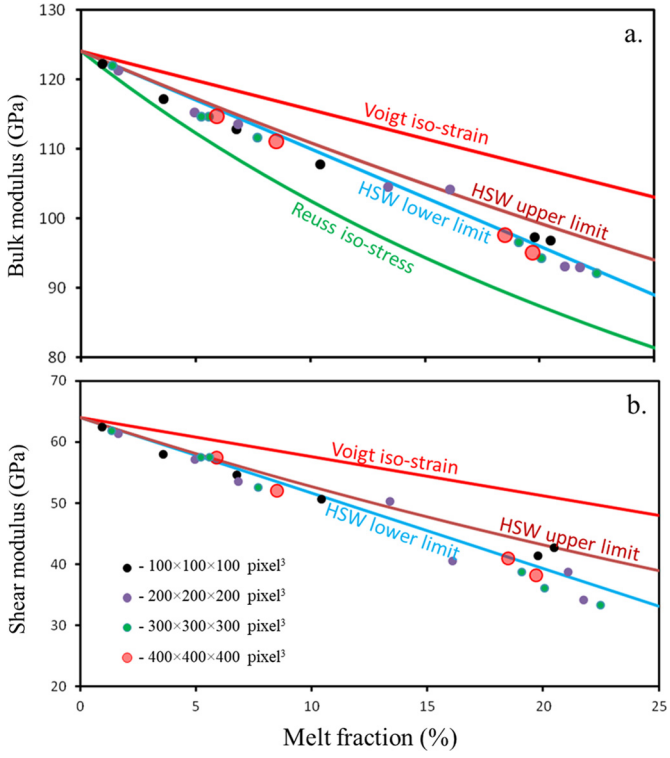

Fig. 2. Elastic moduli, bulk (a) and shear (b) for partially molten rock. HSW - Hashin-Shtrikman-Walpole model.

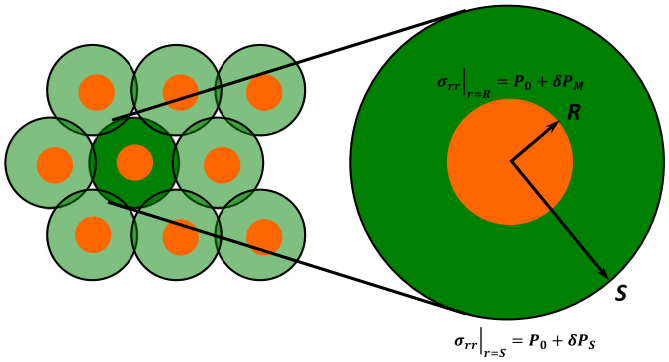

Fig. 3. The cell model for spherical melt inclusions in partially melted rocks (see text for further explanation). R and S are the radii of the inclusion and cell, respectively, σ_{rr} is the radial component of the stress in the cell, P_0 is the equilibrium external pressure, under which the melt inclusion co-exists with the surrounding solid shell, and δP_M and δP_S are the pressure oscillations at the inner and outer solid cell boundaries.

3.2. Analytical solution of solid-melt phase transition, bulk elasticity and wave attenuation

A small wave-induced pressure change at a solid-melt interface disturbs the thermodynamic equilibrium and leads to certain motion of the interface. We develop a model for cyclic loading, with a given amplitude and frequency, keeping in mind effects associated with propagation of monochromatic waves. Transient effects related to a final duration of the wave package and temporal variations of the oscillation amplitudes are not considered here. Pressure and deviatoric stress in the solid phase and pressure in the melt, are coupled by stress continuity at the solid-melt interface during external wave-induced load and fluid pressure oscillations. For a typical wave amplitude of 10^{-5}–10^{-7} m and wavelength between 0.5–5 km, deformations of about 10^{-8}–10^{-10} disturbs the thermodynamic equilibrium. Mathematical formula-

tion of this moving boundary or Stefan problem includes heat, mass, and force balance equations. Any pressure change takes the system out of the thermodynamic equilibrium and causes solidification or melting which change the heat balance according to the Clausius-Clapeyron equation. The latent heat (sink or source) is transferred away or towards the interface by conductive-advective mechanism, heating/cooling the entire rock mass, leading to energy loss and dissipation of the mechanical energy or seismic wave attenuation. An analytical solution is derived for stress distribution and heat exchange between melt inclusion and the solid shell. We neglect the spatial temperature distribution within the small melt inclusion. In larger inclusions, effective mixing of the low viscosity fluid may eliminates any temperature gradients. Therefore we solve for the heat transport only in the solid phase. The analytical solution for the heat balance equation, including latent heat associated with the motion of the solid-melt interface, as well as temperature variations of the melt inclusion, provides the relation between pressure and volumetric strain oscillations. Finally, the derived compressibility of the rock and melt assemblage depends on the characteristics of the external wave-induced forcing. Wave attenuation, or quality factor (Q) is calculated from the time delay between pressure and strain oscillations, or the ratio between real and imaginary bulk moduli.

4. Results

4.1. Solid-melt phase transition, bulk elasticity and wave attenuation

The numerical model simulating the effective elastic properties and the results presented in Fig. 2 are obtained assuming mass conservation of melt and solid phases, without any mass exchange associated with solid-melt phase transition. However, even small wave-induced pressure change at a solid-melt interface disturbs the thermodynamic equilibrium and leads to certain motion of the interface. Pressure changes move the system out of thermodynamic equilibrium, causing solidification or melting which change the heat balance according to the Clausius-Clapeyron equation. The latent heat (sink or source) is transferred away or towards the interface by conductive-advective mechanism, heating or cooling the entire rock mass, leading to energy loss and dissipation of the mechanical energy and to seismic wave attenuation. The presented model is based on the simplified cell geometry representing the partially molten rock as a set of equal elastic cells with spherical melt inclusions (Fig. 3). The simplified cell geometry allows deriving analytical relations for stress distribution and heat exchange between melt inclusion and solid shell, considering three different regimes. Each cell representing the solid-melt system is at initial pressure and temperature (P_0, T_0), corresponding to the thermodynamic equilibrium according to the phase diagram. The propagating pressure wave, with frequency ω and long wavelength (well above the cell size) may be considered as time-dependent pressure perturbations at the outer cell boundary, $P_S(t) = \delta P_S\ e^{i\omega t}$ (Fig. 3). The elastically deformed solid part of the cell transforms this pressure to the melt inclusion with a certain pressure factor ψ, i.e., melt pressure changes proportionally to the pressure wave amplitude, $\delta P_M\ e^{i\omega t} = \psi \cdot \delta P_S\ e^{i\omega t}$, (see Appendix B for complete mathematical derivations). This pressure change destabilizes the thermodynamic equilibrium, which is re-established by the motion of the solid-melt interface. According to the slope of the phase diagram (Clausius-Clapeyron slope, α) the temperature changes proportionally to the pressure, relating the latent heat (heat of phase transformation) to the rate of pressure change with temperature (see Table 1 for notations):

$$\frac{dP}{dT} = \frac{L \cdot \rho^2}{T \cdot \Delta\rho} = \alpha \tag{2}$$

Neglecting the time required to re-establish the thermodynamic equilibrium, the temperature variation at the solid-melt interface is:

$$T_M(t) - T_0 = \psi \delta P_S e^{i\omega t}/\alpha \tag{3}$$

Heat balance associated with moving solid-melt interface includes latent heat and heating/cooling of the melt inclusion and surrounding solid. Heat variation of small melt inclusion is proportional to its mass and temperature variation, while heat flux in the solid part of the cell is proportional to the temperature gradient at the interface. In Appendix B we provide exact solution for the temperature distribution in the solid shell with the oscillating boundary condition (3). The obtained solution, in the form of

$$T(r,t) = \frac{A}{r} e^{ikr} e^{i\omega t} \tag{4}$$

allows calculating the diffusive heat flux towards the solid shell surrounding the melt inclusion:

$$dH = 4\pi\kappa\psi \frac{\delta P_S}{\alpha} R e^{i\omega t}(A_1 + iA_2)dt \tag{5}$$

where

$$\begin{aligned} A_1 &= 1 + \sqrt{\frac{\omega R^2}{2D}} - \left[Cos\left(\sqrt{\frac{\omega}{2D}}(2S-R)\right)\left(1+\sqrt{\frac{2\omega S^2}{D}}\right) \right. \\ &\quad \left. + Sin\left(\sqrt{\frac{\omega}{2D}}(2S-R)\right)\sqrt{\frac{2\omega S^2}{D}} \right] e^{-\sqrt{\frac{\omega}{2D}}(2S-R)} \\ A_2 &= \sqrt{\frac{\omega R^2}{2D}} + \left[Sin\left(\sqrt{\frac{\omega}{2D}}(2S-R)\right)\left(1+\sqrt{\frac{2\omega S^2}{D}}\right) \right. \\ &\quad \left. - Cos\left(\sqrt{\frac{\omega}{2D}}(2S-R)\right)\sqrt{\frac{2\omega S^2}{D}} \right] e^{-\sqrt{\frac{\omega}{2D}}(2S-R)} \end{aligned} \tag{6}$$

Solving the heat balance equation, which also includes latent heat associated with the motion of the solid-melt interface, as well as temperature variations of the melt inclusion, provides the relation between pressure and volumetric strain oscillations. Their ratio ($K = K_R + iK_I = -\delta P_S/\delta\varepsilon_V$) is the complex bulk modulus:

$$K = \left\{ \frac{1}{K_e} + \frac{\beta\gamma\psi}{\alpha L \rho_S}\left[\rho_M C_P + (A_2 - iA_1)\frac{3\kappa}{\omega R^2} \right] \right\}^{-1} \tag{7}$$

The ratio K_R/K_I between the real and imaginary parts of the bulk modulus (7) defines the bulk quality factor, Q, of the media (see Appendix B)

$$Q = \frac{\alpha L \rho_S \omega R^2 + \beta\gamma\psi K_e \rho_M C_P \omega R^2 + \beta\gamma\psi K_e A_2 3\kappa}{K_e \beta\gamma\psi A_1 3\kappa} \tag{8}$$

These derivations demonstrate that moving solid-melt phase boundary due to wave-induced pressure oscillations leads to additional reduction of the bulk modulus, K_e, estimated from the elastic deformation, and provides efficient mechanism for wave attenuation. Most of the material properties in (6), (7), (8) are well defined with relatively small uncertainty range (e.g., Ricard, 2015). The exception is the product of the Clausius-Clapeyron slope and latent heat values, which according to (2) is expressed as:

$$\alpha L = \frac{\alpha^2 T \Delta\rho}{\rho^2} \tag{9}$$

Table 1
Values of the model constants.

Notation	Parameter	Value/units
K_S	Solid bulk modulus	124 GPa
μ_S	Solid shear modulus	64 GPa
ν_S	Solid Poisson ratio	0.28
K_M	Melt bulk modulus	40 GPa
K_e	Effective bulk modulus	GPa
μ_e	Effective shear modulus	GPa
β	Melt fraction	0-20%
α	Clausius-Clapeyron slope	1-10 MPa/°K
κ	Heat conductivity	3.5 J/s m °K
C_p	Heat capacity	1 kJ/kg °K
L	Specific latent heat	10^2-10^3 kJ/kg
ρ_S	Solid density	3,500 kg/m^3
ρ_M	Melt density	3,000 kg/m^3
$D = \frac{\kappa}{\rho_S C_P}$	Thermal diffusivity	1×10^{-6} m^2/s
S_0	Cell radius	0.5-5 $\times 10^{-3}$ m
$R = S_0 \sqrt[3]{\beta}$	Inclusion radius	M
γ	Volumetric strain factor	0.25
ψ	Pressure factor	0.54

Therefore, we ignore the uncertainty in most of the parameters presented in Table 1, and study the sensitivity of the model predictions to the reasonable variations of the Clausius-Clapeyron slope values $\alpha = 3,\ 6,\ 9$ MPa/°K (Bina and Helffrich, 1994). Larger slope values, from ~7.5 MPa/°K at low pressures up to ~30 MPa/°K at 10 GPa were reported by (Hirschmann, 2000) for various compositions of mantle Peridotites.

Fig. 4 shows reduction of the bulk modulus as a function of the melt fraction calculated using eq. (7). We define the cell-size, as the typical distance between melt pockets. In brittle rheology, these melt pockets are typically grain-size away from each other, while for ductile rheology they would be further separated. For small cell-size (Fig. 4a for $S_0 = 0.5$ mm) the reduction is larger than for relatively large cell-size (Fig. 4b for $S_0 = 5.0$ mm). In both cases smaller Clausius-Clapeyron slope values lead to more significant effect, since the amplitude of the temperature oscillations at the solid-melt interface (3) is proportional to $1/\alpha$. The most pronounced change above 80% reduction occurs at low melt fraction values below 2% for $\alpha = 3$ and 6 MPa/°K (Fig. 4a) and then remains about constant. Larger cell-size (Fig. 4b) causes gradual reduction of the bulk modulus. Values of the quality factor (Q) for 1 Hz p-wave frequency, calculated using eq. (8), also strongly depend on these factors (Fig. 5). For small grain size ($S_0 = 0.5$ mm) the reduction is practically abrupt at very low melt fraction values and then Q remains practically constant within the values shown by the red polygon in Fig. 5. For larger $S_0 = 5.0$ mm, the Q decrease is steeper for small α-values and approach about constant value at melt fraction values above ~5%. Since the presented model ignores wave attenuation in the solid phase, the Q-values go to infinity for zero melt fraction value ($\beta = 0$).

Wave attenuation predicted by the model, is strongly frequency-dependent (Fig. 6). Less attenuation or higher Q-values are obtained at very low and high frequency values. If the oscillation period is very large, the whole cell volume is heated to the equilibrium temperature and the delay associated with heat transfer is small. Similarly, heat transfer can be neglected at very small period values. The highest attenuation occurs when the period of oscillation is close to the heat transfer time scale. In this condition, any heating that occurs due to solid-melt phase transition during the oscillation affects the entire cell and therefore causes high attenuation. The time needed to transfer heat over the cell size or the characteristic time scale of conductive heat transfer over the cell size is defined as $S_0^2 D$. Therefore, the largest attenuation occurs when $f \cdot S_0^2/D \sim 1$. For small cell-size (Fig. 6a) maximum attenuation is expected at frequency range, f, between 1 and 10 Hz. Q-values are very low and weakly depend on the melt fraction.

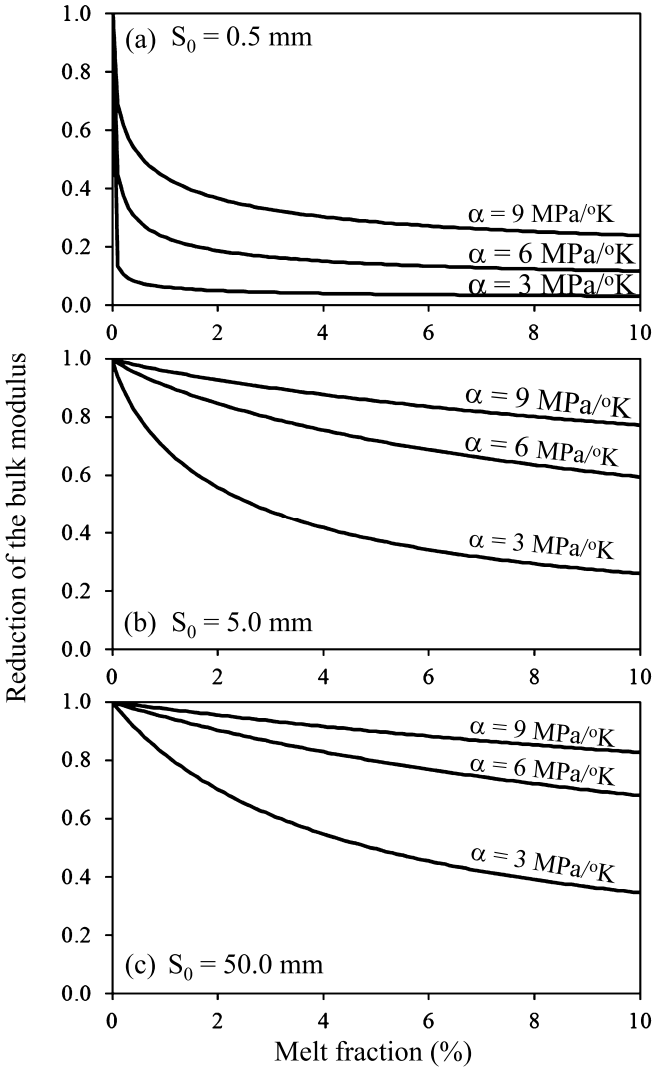

Fig. 4. Reduction of the bulk modulus versus melt fraction for different Clausius-Clapeyron slope values a = 3, 6, and 9 MPa/°K; $S_0 = 0.5$ mm (a), 5.0 mm (b), and 50.0 mm (c), and 1 Hz frequency.

One order of magnitude increase in the cell-size causes two orders of magnitude (S_0^2) frequency change (0.01–0.1 Hz) for maximum attenuation (Fig. 6b). In both cases, the increase in Q-values at low frequencies only weakly depends on the melt fraction, while it is significantly more sensitive at high frequencies.

5. Discussion

Understanding how magma or molten rocks are stored at depth is one of the major challenges in volcanology, igneous geology, mantle dynamics, and plate tectonics. Many of the ongoing geodynamic key processes and related natural hazards require information on the distribution of partial melt storage system and of reservoirs in the Earth's crust and upper mantle. Seismological methods are often used to show areas of significant reduction in seismic wave velocities and enhanced wave attenuation, and are interpreted as revealing pockets of partially molten rocks. Interpretation of the seismological observations requires understanding the effects of partial molten rock properties on the melt fraction and on the topology of melt inclusions.

Previous studies show that viscous dissipation due to flow or squirt of the melt with realistic viscosity range is small and ex-

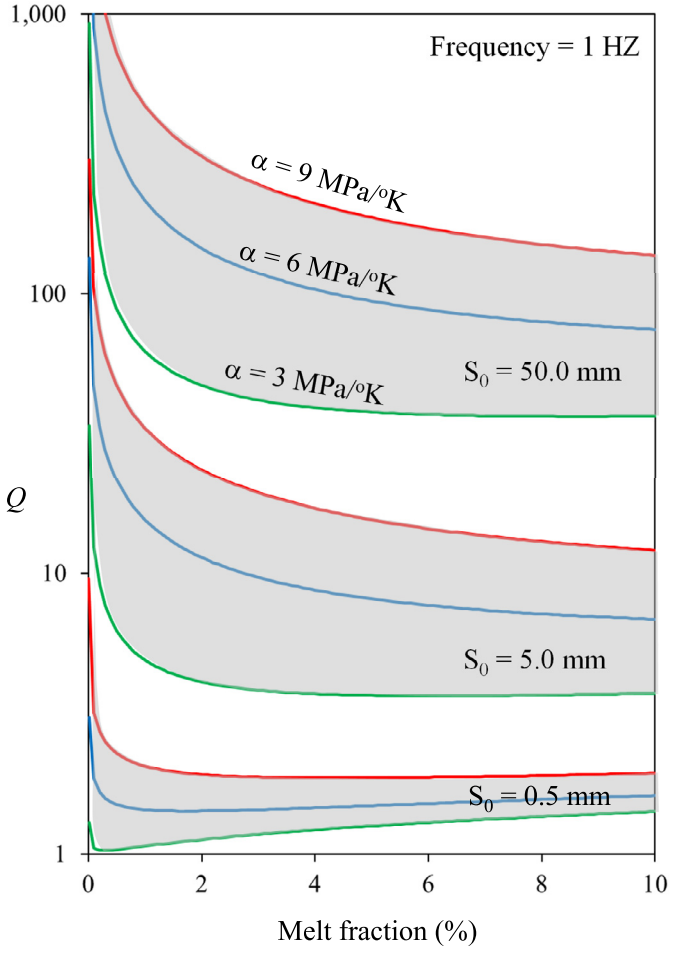

Fig. 5. Q versus melt fraction for different Clausius-Clapeyron slope values $\alpha = 9$ MPa/°K (red lines), $\alpha = 6$ MPa/°K (blue lines), and $\alpha = 3$ MPa/°K (green lines). Shaded polygons show Q-values for different values of $S_0 = 0.5$ mm, 5.0 mm, and 50.0 mm.

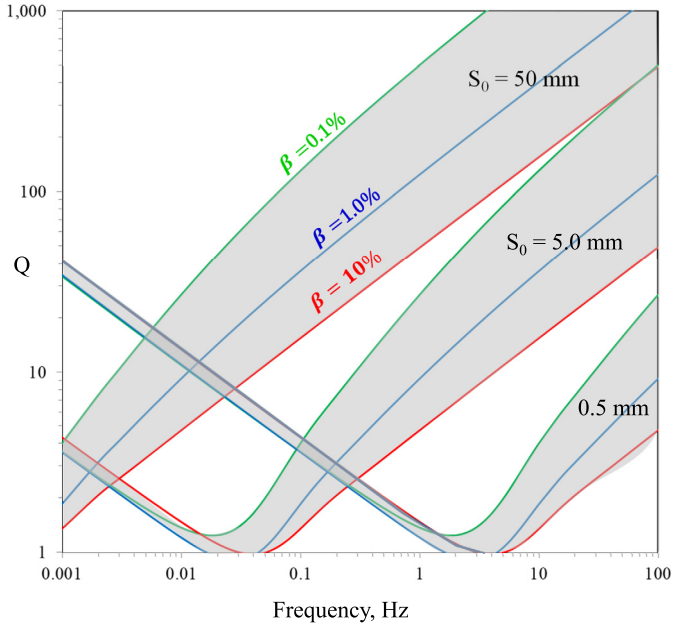

Fig. 6. Q versus frequency for different melt fraction values b = 0.1%, 1.0%, and 10% and Clausius-Clapeyron slope value a = 5 MPa/°K. Shaded polygons show Q-values for $S_0 = 0.5$ mm, 5.0 mm, and 50.0 mm.

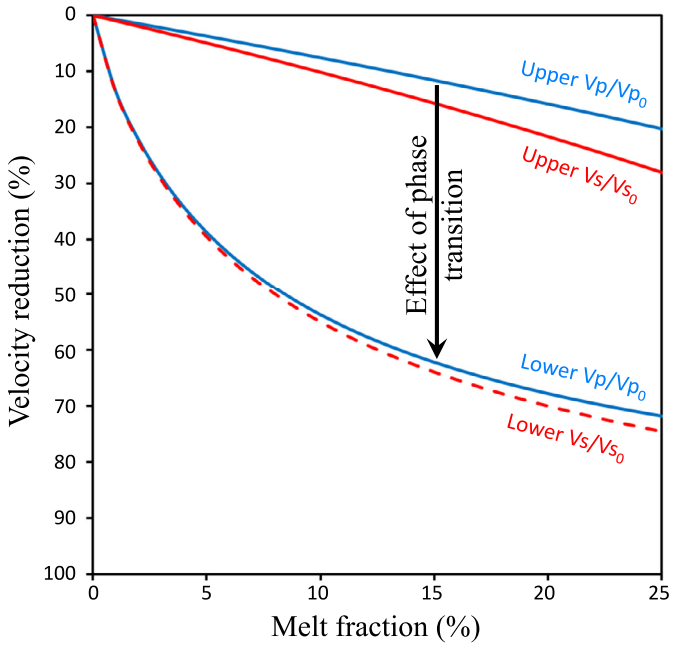

Fig. 7. Velocity change predicted by the model with spherical inclusions and corrected after the phase transition effect for $S_0 = 5.0$ mm, a = 5 MPa/°K, and 1 Hz frequency.

pected attenuation is well below the typical values for the partially molten rocks. The developed analytical model shows that phase transition is an efficient mechanism for strong attenuation and for the reduction of wave velocity. The model adopts cell geometry for spherical melt inclusions in partially molten rocks (Fig. 3). Previous results demonstrate that in spite of a complex melt topology, this simple geometrical model provides surprisingly good approximation for the effective rock elasticity. This important result allows using analytical solutions, assuming spherical inclusions, for estimating effective elastic properties and modeling wave attenuation.

The most realistic bounds, providing the narrowest possible range of bulk elasticity, leaving solid-melt phase transition out of the consideration, is the Hashin–Shtrikman–Walpole model. Their model predicts relatively minor reduction in both pressure and shear wave velocities with melt fraction (Fig. 7). However, even for relatively large cell-size ($S_0 = 5$ mm) and intermediate Clausius-Clapeyron slope value, $\alpha = 5$ MPa/°K, the reduction in the bulk modulus associated with the phase transition is dominant (Fig. 7). The analytical solution considers only spherical symmetry and volumetric deformation, and formally cannot relate phase transition to shearing, which in perfect material is decoupled from volumetric deformation. However, original studies by Reynolds (1885) and Skempton (1954), have shown that shear stress is strongly coupled with pressure, and therefore the formal decoupling is in doubt. Taking into account the relation between S-wave induced shearing and pressure, we speculate here that propagating S-waves will also lead to similar phase boundary motion, i.e., velocity reduction and attenuation. Dashed red line in Fig. 7 shows the inferred shear modulus reduction using the same factor as for the P-waves. More accurate relations for the S-waves will be examined in future study.

In summary, the analyzed mechanism of reduction in mechanical properties associated with the phase transition predicts that the presence of significant amount of melt in the rocks would result in a strong decrease in seismic wave velocities associated with a strong increase of their attenuation. Preliminary consideration also indicates that the velocity decrease should be more enhanced for S wave (Fig. 7), resulting in the increase of the Vp/Vs ratio.

This implies that simultaneous measurement of these properties could help to better constrain the melt content in studied geological objects such as, for example, volcanic systems. A key parameter for interpretation of such results is the average cell-size S_0, that remains poorly known. Results shown in Fig. 6 indicate that this parameter cannot be too small (<1 mm) because in this case the waves at frequencies between 1 and 10 Hz (i.e. typical range of observation for volcanic earthquakes) would be completely dissipated ($Q < 5$). Considering the millimeter or centimeter scale of the melt distribution spatial heterogeneity would result in more appropriate predictions, with Q varying between 10 and several hundreds at 1 Hz. Moreover, with such values of S_0, the model predicts approximately a power-law increase of Q at high frequencies, i.e., the behavior reported from field observations and laboratory experiments (Lekić et al., 2009). In addition, decaying waveform packets at a range of frequencies, as seen in seismic observations, may reflect higher Q values, resulting from the superposition at a range of frequencies. Overall, the predicted values are in general agreement with large scale seismological observations showing that seismic waves are mostly attenuated within the shallow parts of the Earth's crust and mantle, and associated with possible presence of melt, such as in mid-oceanic ridges and island arcs or beneath large volcanic systems. The model is also in agreement with observed significant correlation between the regional-scale tectonics and the geographical distributions of uppermost-mantle velocities and attenuation for S and P waves. So far, average Q, being as low as ~60, has been observed in the upper mantle low velocity zone, where significant amount of melt may be expected (e.g., Thybo, 2006). Comparison of this observation with Fig. 6 would suggest that average melt fraction does not exceed 1% because with more melt our model would predict Q values smaller than 50. Such extreme values are observed only within relatively small volumes in specific extremely melt-rich environments such as rift zones beneath mid-oceanic ridges (Eilon and Abers, 2017) or volcano plumbing systems (Lin et al., 2015).

The presented model considers latent heat generation at the solid-melt phase transition and heat transport near the interface. Adopting infinitely fast kinetics, the model predicts realistic body wave attenuation within frequency range of 0.1–1 Hz. The alternative approach, considering solid-solid transition with finite phase (Durand et al., 2012; Ricard et al., 2009), predicts maximum attenuation at significantly lower frequency range typical for free oscillations. The real case might be somewhat in-between and the complete model should consider both types of phase transitions.

6. Conclusion

In spite of the complex structure of partially molten rocks, effective elastic moduli can be approximated assuming spherical melt inclusions geometry, which implies that the exact topology of the melt even at high melt fraction values is not crucial. Viscous flow mechanisms for basaltic melts can cause attenuation only at very high-frequency waves. Explaining observed wave attenuation in partially molten peridotite rocks using viscous flow requires adjusting unrealistically high viscosities.

We present a new mechanism for wave velocity reduction and attenuation associated with moving solid-melt interface (Stefan problem), and latent heat generation due to wave-induced pressure oscillations around thermodynamic equilibrium. The reduction in mechanical properties (seismic velocities) associated with the phase transition is shown to be significant. The highest attenuation occurs when the period of oscillation is close to the heat transfer time-scale. In this condition, any heating that occurs due to Solid-melt phase transition during the oscillation is affecting the entire cell and therefore causes high attenuation.

CRediT authorship contribution statement

Vladimir Lyakhovsky: Conceptualization, Methodology, Writing – original draft. **Eyal Shalev:** Conceptualization, Visualization. **Ittai Kurzon:** Methodology, Writing – review & editing. **Wenlu Zhu:** Methodology. **Laurent Montesi:** Methodology. **Nikolai M. Shapiro:** Writing – review & editing.

Declaration of competing interest

The authors declare that they have no known competing financial interests or personal relationships that could have appeared to influence the work reported in this paper.

Acknowledgements

We thank Navot Morag for discussions. The paper benefited from useful comments by Hans Thybo, Claude Jaupart and an anonymous reviewer. The study was supported by grant from the United States-Israel Binational Science Foundation (BSF 2014036). This study was supported by the Russian Ministry of Education and Science (Grant 14.W03.31.0033) and by the European Research Council under the European Union Horizon 2020 research and innovation program (Grant Agreement 787399-SEISMAZE). WZ and LM acknowledge supports from the US National Science Foundation under grants EAR-1761912 and EAR-1629356.

Appendix A. Supplementary material

Supplementary material related to this article can be found online at https://doi.org/10.1016/j.epsl.2021.117117.

References

Allen, R.M., Nolet, G., Morgan, W.J., Vogfjörd, K., Bergsson, B.H., Erlendsson, P., Foulger, G.R., Jakobsdóttir, S., Julian, B.R., Pritchard, M., 2002. Imaging the mantle beneath Iceland using integrated seismological techniques. J. Geophys. Res., Solid Earth 107, ESE-3.

Asimow, P.D., Langmuir, C.H., 2003. The importance of water to oceanic mantle melting regimes. Nature 421, 815–820.

Baba, K., Chave, A.D., Evans, R.L., Hirth, G., Mackie, R., 2006. Mantle dynamics beneath the East Pacific rise at 17 S: insights from the mantle electromagnetic and tomography (MELT) experiment. J. Geophys. Res., Solid Earth 111.

Bina, C.R., Helffrich, G., 1994. Phase transition Clapeyron slopes and transition zone seismic discontinuity topography. J. Geophys. Res., Solid Earth 99, 15853–15860.

Bryan, S.E., Peate, I.U., Peate, D.W., Self, S., Jerram, D.A., Mawby, M.R., Marsh, J.S.G., Miller, J.A., 2010. The largest volcanic eruptions on Earth. Earth-Sci. Rev. 102, 207–229.

Campbell, I., 2005. Large igneous provinces and the mantle plume hypothesis. Elements 1, 265–269.

Chantel, J., Manthilake, G., Andrault, D., Novella, D., Yu, T., Wang, Y., 2016. Experimental evidence supports mantle partial melting in the asthenosphere. Sci. Adv. 2, e1600246.

Chen, J., Gaillard, F., Villaros, A., Yang, X., Laumonier, M., Jolivet, L., Unsworth, M., Hashim, L., Scaillet, B., Richard, G., 2018. Melting conditions in the modern Tibetan crust since the miocene. Nat. Commun. 9, 1–13.

Chouet, B., 1996. Long-period volcano seismicity: its source and use in eruption forecasting. Nature 380, 309–316.

Conder, J.A., Forsyth, D.W., Parmentier, E.M., 2002. Asthenospheric flow and asymmetry of the East Pacific rise, MELT area. J. Geophys. Res., Solid Earth 107, ETG-8.

Debayle, E., Bodin, T., Durand, S., Ricard, Y., 2020. Seismic evidence for partial melt below tectonic plates. Nature 586, 555–559.

Di Toro, G., Hirose, T., Nielsen, S., Pennacchioni, G., Shimamoto, T., 2006. Natural and experimental evidence of melt lubrication of faults during earthquakes. Science 80 (311), 647–649.

Durand, S., Chambat, F., Matas, J., Ricard, Y., 2012. Constraining the kinetics of mantle phase changes with seismic data. Geophys. J. Int. 189, 1557–1564.

Eilon, Z.C., Abers, G.A., 2017. High seismic attenuation at a mid-ocean ridge reveals the distribution of deep melt. Sci. Adv. 3, e1602829. https://doi.org/10.1126/sciadv.1602829.

Ekström, G., Dziewonski, A.M., 1998. The unique anisotropy of the Pacific upper mantle. Nature 394, 168–172.

Faul, U., Jackson, I., 2015. Transient creep and strain energy dissipation: an experimental perspective. Annu. Rev. Earth Planet. Sci. 43, 541–569. https://doi.org/10.1146/annurev-earth-060313-054732.

Faul, U.H., Fitz, G.J.D., Jackson, I., 2004. Shear wave attenuation and dispersion in melt-bearing olivine polycrystals: 2. Microstructural interpretation and seismological implications. J. Geophys. Res., Solid Earth 109.

Fontaine, F.R., Ildefonse, B., Bagdassarov, N.S., 2005. Temperature dependence of shear wave attenuation in partially molten gabbronorite at seismic frequencies. Geophys. J. Int. 163, 1025–1038. https://doi.org/10.1111/j.1365-246X.2005.02767.x.

Gerya, T., Meilick, F.I., 2011. Geodynamic regimes of subduction under an active margin: effects of rheological weakening by fluids and melts. J. Metamorph. Geol. 29, 7–31.

Hammond, W.C., Humphreys, E.D., 2000. Upper mantle seismic wave velocity: effects of realistic partial melt geometries. J. Geophys. Res., Solid Earth 105, 10975–10986.

Hill, G.J., Caldwell, T.G., Heise, W., Chertkoff, D.G., Bibby, H.M., Burgess, M.K., Cull, J.P., Cas, R.A.F., 2009. Distribution of melt beneath Mount St Helens and Mount Adams inferred from magnetotelluric data. Nat. Geosci. 2, 785–789.

Hirschmann, M.M., 2000. Mantle solidus: experimental constraints and the effects of peridotite composition. Geochem. Geophys. Geosyst. 1.

Jackson, I., Faul, U.H., Fitz, G.J.D., Tan, B.H., 2004. Shear wave attenuation and dispersion in melt-bearing olivine polycrystals: 1. Specimen fabrication and mechanical testing. J. Geophys. Res., Solid Earth 109.

Jackson, M.D., Blundy, J., Sparks, R.S.J., 2018. Chemical differentiation, cold storage and remobilization of magma in the Earth's crust. Nature 564, 405–409.

Jaxybulatov, K., Shapiro, N.M., Koulakov, I., Mordret, A., Landès, M., Sens-Schönfelder, C., 2014. A large magmatic sill complex beneath the Toba caldera. Science 346 (6209), 617–619.

Karato, S.-I., Spetzler, H.A., 1990. Defect microdynamics in minerals and solid-state mechanisms of seismic wave attenuation and velocity dispersion in the mantle. Rev. Geophys. 28, 399–421.

Koulakov, I., Shapiro, N.M., Sens-Schönfelder, C., Luehr, B.G., Gordeev, E.I., Jakovlev, A., Abkadyrov, I., Chebrov, D.V., Bushenkova, N., Droznina, S.Y., 2020. Mantle and crustal sources of magmatic activity of Klyuchevskoy and surrounding volcanoes in Kamchatka inferred from earthquake tomography. J. Geophys. Res., Solid Earth 125, e2020JB020097.

Lekić, V., Matas, J., Panning, M., Romanowicz, B., 2009. Measurement and implications of frequency dependence of attenuation. Earth Planet. Sci. Lett. 282, 285–293.

Li, L., Weidner, D.J., 2008. Effect of phase transitions on compressional-wave velocities in the Earth's mantle. Nature 454, 984–986. https://doi.org/10.1038/nature07230.

Lin, G., Shearer, P.M., Amelung, F., Okubo, P.G., 2015. Seismic tomography of compressional wave attenuation structure for Kılauea Volcano, Hawai 'i. J. Geophys. Res., Solid Earth 120, 2510–2524.

Mavko, G., 1980. Velocity and attenuation in partially molten rocks. J. Geophys. Res., Solid Earth 85, 5173–5189.

Mavko, G., Mukerji, T., Dvorkin, J., 2009. The Rock Physics Handbook, second edition. Cambridge University Press.

Miller, K.J., Zhu, W., Montési, L., Gaetani, G.A., 2014. Experimental quantification of permeability of partially molten mantle rock. Earth Planet. Sci. Lett. 388, 273–282.

Morris, S.J.S., Jackson, I., 2009. Diffusionally assisted grain-boundary sliding and viscoelasticity of polycrystals. J. Mech. Phys. Solids 57 (4), 744–761. https://doi.org/10.1016/j.jmps.2008.12.006.

Niu, Y., 1997. Mantle melting and melt extraction processes beneath ocean ridges: evidence from Abyssal peridotites. J. Petrol. 38, 1047–1074. https://doi.org/10.1093/petroj/38.8.1047.

O'Connell, R.J., Budiansky, B., 1977. Viscoelastic properties of fluid-saturated cracked solids. J. Geophys. Res. 82, 5719–5735.

Pinel, V., Jaupart, C., Albino, F., 2010. On the relationship between cycles of eruptive activity and growth of a volcanic edifice. J. Volcanol. Geotherm. Res. 194, 150–164.

Prudencio, J., Manga, M., 2020. 3-D seismic attenuation structure of Long Valley caldera: looking for melt bodies in the shallow crust. Geophys. J. Int. 220, 1677–1686.

Reuss, A., 1929. Berechnung der fließgrenze von mischkristallen auf grund der plastizitätsbedingung für einkristalle. Z. Angew. Math. Mech. 9, 49–58.

Reynolds, O., 1885. LVII. On the dilatancy of media composed of rigid particles in contact. Philos. Mag. 20, 469–481. With experimental illustrations.

Ricard, Y., 2015. 7.02 - physics of mantle convection. In: Schubert, G. (Ed.). Elsevier, Oxford, pp. 23–71.

Ricard, Y., Matas, J., Chambat, F., 2009. Seismic attenuation in a phase change coexistence loop. Phys. Earth Planet. Inter. 176, 124–131. https://doi.org/10.1016/j.pepi.2009.04.007.

Rychert, C.A., Laske, G., Harmon, N., Shearer, P.M., 2013. Seismic imaging of melt in a displaced Hawaiian plume. Nat. Geosci. 6, 657–660.

Shapiro, N.M., Droznin, D.V., Droznina, S.Y., Senyukov, S.L., Gusev, A.A., Gordeev, E.I., 2017. Deep and shallow long-period volcanic seismicity linked by fluid-pressure transfer. Nat. Geosci. 10, 442–445.

Skempton, A.W., 1954. The pore-pressure coefficients A and B. Geotechnique 4, 143–147.

Sobolev, S.V., Sobolev, A.V., Kuzmin, D.V., Krivolutskaya, N.A., Petrunin, A.G., Arndt, N.T., Radko, V.A., Vasiliev, Y.R., 2011. Linking mantle plumes, large igneous provinces and environmental catastrophes. Nature 477, 312–316.

Thybo, H., 2006. The heterogeneous upper mantle low velocity zone. Tectonophysics 416, 53–79. https://doi.org/10.1016/j.tecto.2005.11.021.

Vaišnys, J.R., 1968. Propagation of acoustic waves through a system undergoing phase transformations. J. Geophys. Res. 73, 7675–7683.

van Hunen, J., Zhong, S., Shapiro, N.M., Ritzwoller, M.H., 2005. New evidence for dislocation creep from 3-D geodynamic modeling of the Pacific upper mantle structure. Earth Planet. Sci. Lett. 238, 146–155.

Voigt, W., 1890. Bestimmung der Elasticitätsconstanten des brasilianischen Turmalines. Ann. Phys. 277, 712–724. https://doi.org/10.1002/andp.18902771205.

Watanabe, T., Kurita, K., 1993. The relationship between electrical conductivity and melt fraction in a partially molten simple system: Archie's law behavior. Phys. Earth Planet. Inter. 78, 9–17.

Yamauchi, H., Takei, Y., 2016. Polycrystal anelasticity at near-solidus temperatures. J. Geophys. Res., Solid Earth 121, 7790–7820. https://doi.org/10.1002/2016JB013316.

Zhu, W., Gaetani, G.A., Fusseis, F., Montési, L.G.J., De Carlo, F., 2011. Microtomography of partially molten rocks: three-dimensional melt distribution in mantle peridotite. Science 332 (6025), 88–91. https://doi.org/10.1126/science.1202221.

Zhu, W., et al. Effective Seismic Wave Velocity of Partially Molten Upper Mantle Rocks. In preparation.